Part II Applied Physics

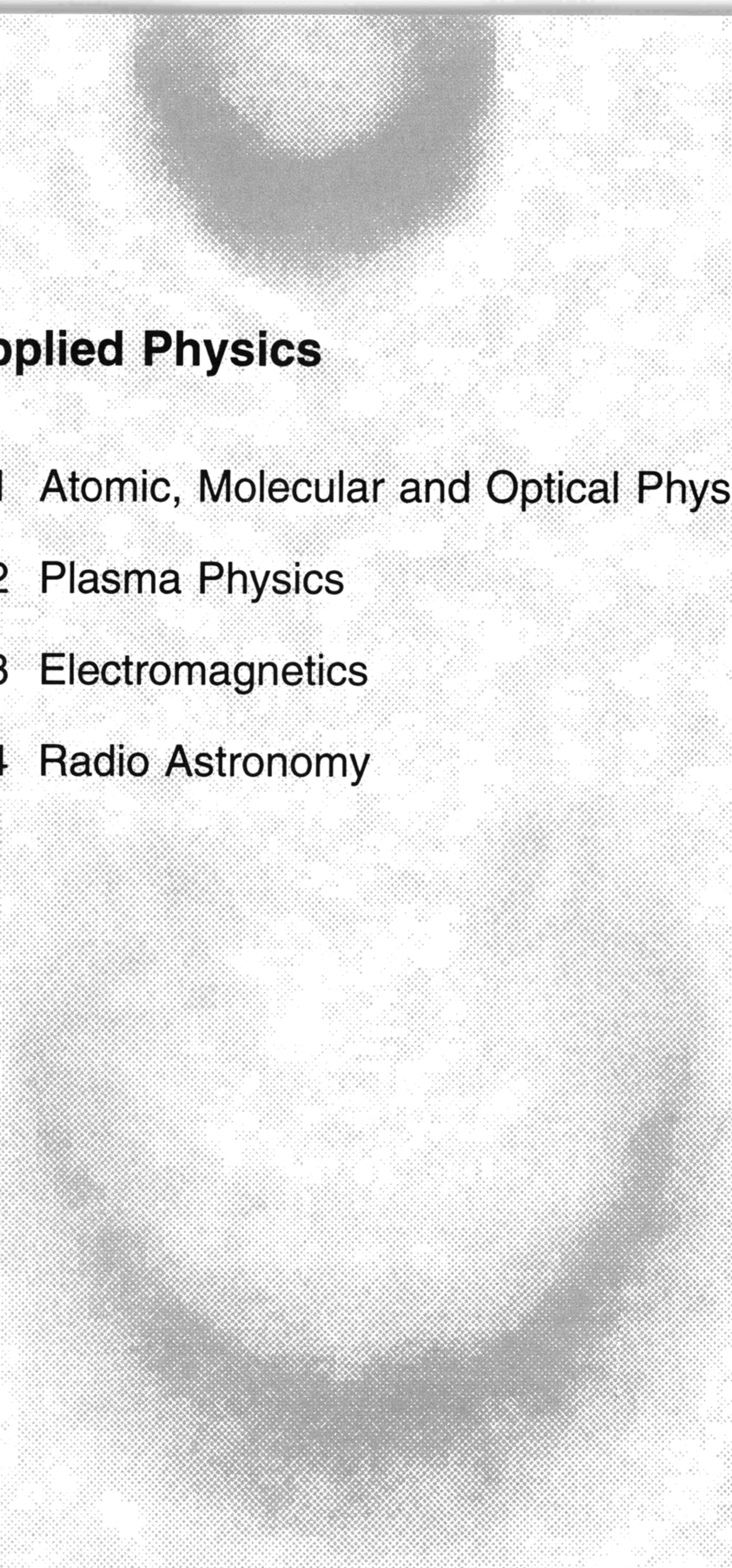

Section 1 Atomic, Molecular and Optical Physics

Chapter 1. Quantum Optics and Photonics

Academic and Research Staff

Professor Shaoul Ezekiel, Dr. Selim M. Shahriar, Dr. Stephen P. Smith, Dr. Byoung S. Ham, Dr. Venkatapuram S. Sudarshanam, Dr. Xiao-Wei Xia

Visiting Scientists and Research Affiliates

Dr. M. Cronin-Golomb, Dr. Timothy T. Grove, Dr. Philip R. Hemmer,[1] Michelle Henrion, Dr. Chris Leung, Dr. Mara G. Prentiss,[2] John D. Kierstead[1]

Graduate Students

John J. Donoghue,[3] Niell G. Elvin, Yuli Friedman, Darren S. Hsiung, Emmanuel Rousseau

Undergraduate Students

Steve S. Paik, Perry I. Tsao

1.1 Efficient, Fast, Low-Power Optical Phase Conjugation Using Two-Photon-Induced Zeeman Coherence in Rubidium for Spatially Broadband Squeezing

Sponsors

National Research Council
  Postdoctoral Fellowship
U.S. Air Force - Electronic Systems Division
  Contract F30602-96-2-0100
U.S. Air Force - Office of Scientific Research/
  AASERT
  Contract F49620-96-1-0308
U.S. Air Force - Office of Scientific Research/
  DURIP
  Grant F49620-95-1-0510

Optical phase conjugation (OPC) has great potential for numerous applications. However, current OPC materials limit the usefulness of this technique. Photo-refractives (such as $BaTiO_3$) have high gain at low pump intensities (reflectivity greater than 10 at pump powers less than 1 W/cm^2). However, the response time for photo-refractives (~10 msec) is not fast enough to correct for high-speed turbulence. Two-level atomic vapors have produced fast response times (10-100 nsec) with a high reflectivity, but only at high power. The ultimate goal in the search for a phase conjugator material is to achieve a fast response time and a high reflectivity at a low pump power, without causing overwhelming technical difficulties.

In the past, we demonstrated a high-gain optical phase conjugator in sodium vapor with a fast response time, distortion-free propagation and low pump intensities.[4] This optical phase conjugator, based on coherent population trapping (CPT), meets most goals (reflectivity greater than 50 with a response time less than 1 μsec at a pump power of 1 W/cm^2). However, for practical devices there are several problems with this system. The two pump beams need to be detuned nearly 1.77 GHz. This is compounded by the subnatural linewidth (for the detuning between the forward pump and signal beam) associated with coherent population trapping. Second, bulky dye lasers are used to produce the 589 nm wavelength at the necessary power for sodium. Other alkali vapors (such as Rb

---

[1] Rome Laboratory, Hanscom Air Force Base, Bedford, Massachusetts.

[2] Professor, Department of Physics, Harvard University, Cambridge, Massachusetts.

[3] Electro-optics Center, Tufts University, Medford, Massachusetts.

[4] P.R. Hemmer, D.P. Katz, J. Donoghue, M. Cronin-Golomb, M.S. Shahriar, and P. Kumar, *Opt. Lett.* 20: 982 (1995); T.T. Grove, M.S. Shahriar, P.R. Hemmer, P. Kumar, V.K. Sudarshanam, and M. Cronin-Golomb, "Distortion-Free Gain and Noise Correlation in Sodium Vapor Using Four Wave Mixing and Coherent Population Trapping," *Opt. Lett.*, forthcoming.

and Cs) have transitions accessible by diode lasers, but the problem of a large detuning (3.0 GHz for ^{85}Rb, 6.8 GHz for ^{87}Rb, 9.2 GHz for Cs) with a subnatural linewidth still remains.[5] A practical system would not be tied to a particular hyperfine ground state splitting or for that matter an alkali transition wavelength.

Recently, we have produced Λ systems using Zeeman sublevels in a vapor cell. Coherences between Zeeman split ground state levels have been used in a variety of experiments.[6] The energy levels involved are illustrated in figure 1. The obvious advantage is that there is no large detuning between the beams that excite the two legs of the Λ system. A more subtle advantage is that almost any transition in any atomic vapor can work. Since a typical hyperfine ground state splitting is large compared to the Maxwell-Boltzmann profile (of a single ground state transition) in a vapor cell, atoms in the unused hyperfine ground state are transparent. Second, natural re-pump processes in a cell (e.g., collisions with other atoms and walls) can provide a continuous sample of atoms with the desired hyperfine ground state. Thus, by varying the vapor's temperature, we can obtain the necessary number of atoms in the wanted hyperfine ground state. In this work, we concentrate on the ^{87}Rb $5^2S_{1/2}$ F = 2 → $5^2P_{1/2}$ F = 1 transition (see figure 1). There is nothing special about this transition, and we also observed robust conjugates for other rubidium transitions (as well as ^{85}Rb transitions). For the sake of simplicity, figure 1 includes only one of the possible Λ systems, and the frequency and polarization dependence of each beam is indicated. The forward beam, F, and the signal beam, S, produce a grating via coherent population trapping. The backward beam, B, diffracts off this grating, forming the conjugate beam. The polarizations are now critical to ensure the formation of the Λ systems.

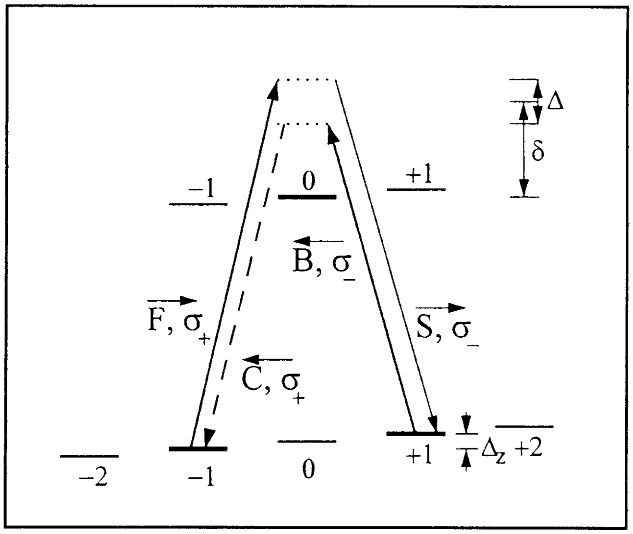

Figure 1. Illustration of the four-wave mixing interaction in the ^{87}Rb $5^2S_{1/2}$ F = 2 → $5^2P^{1/2}$ F = 1 transition. Only one of the possible Λ systems is shown. The polarization and relative detunings of each beam is shown.

Figure 2 demonstrates how we produce the beams for this experiment. All beams originate from a single Ti:Sapphire laser. We use a λ/2 plate and a polarizing beam-splitting cube as a variable power attenuator. Two AOMs produce the pump beams (F and B). The signal beam, S, is produced from a small percentage of the forward beam. We use two more AOMs in order to produce a small frequency difference between the signal beam and the forward beam. This frequency difference is zero (at zero magnetic field) for peak efficiency and is introduced only for diagnostic purposes. The four-wave mixing occurs in a rubidium heat pipe oven at an approximate temperature of 140 degrees C. Typically the two pumps had a 1 mm FWHM, while the signal had a FWHM of 0.6 mm. All beams cross with angles below few mrads. To obtain the correct polarizations, we use a series of λ/2 plates, λ/4 plates, and a polarizing beam splitting cubes. The forward beam passes through a λ/2 plate that optimizes the transmission through the beam-splitting cube. A λ/4 plate produces circular polarization (σ_+) in the Rb cell and a second λ/4 plate (after the cell) optimizes transmission through the second cube. By arranging the λ/4 plates and beam-splitting cubes in this way, the signal beam obviously has the opposite polarization at the cell (σ_-) and reflects off the second cube. The backward beam (which transmits through the cube) also has σ_- polarization. We measure the power in each beam after

---

[5] O.S. Heavens, *J. Opt. Soc. Am.* 51: 1058 (1961).

[6] W. Gawlik, J. Kowalski, F. Trager, and M. Vollmer, *Phys. Rev. Lett.* 48: 871 (1982); D. Suter, M. Rosatzin, and J. Mlynek, *Phys. Rev. Lett.* 67: 34 (1991); D. Suter, H. Klepel, and J. Mlynek, *Phys. Rev. Lett.* 67: 2001 (1991).

the cubes with photodiodes. Since a two-level system conjugate could also conceivably form, we use two photodiodes to detect the conjugate. A two-level system conjugate must have the same polarization as the signal beam (σ_-), which would transmit through the cube (C' in figure 2). The part of the conjugate that reflects at the cube is due to the Λ systems.

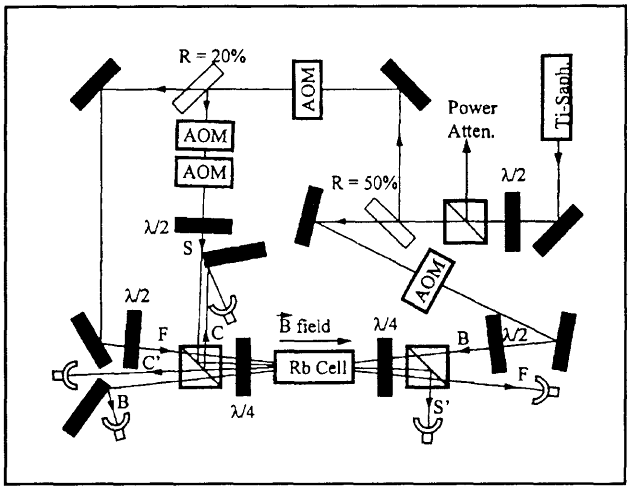

Figure 2. Schematic illustration of the experimental set-up for producing phase conjugates using a heat pipe oven.

Figure 3 demonstrates the frequency dependence of the conjugate as we scan the Ti:Sapphire laser from the ^{87}Rb $5^2S_{1/2}$ F = 2 → $5^2P_{1/2}$ F = 1 transition to the $5^2P_{1/2}$ F = 2 transition. The power is in units of the input signal power, and the two resonances are marked at the bottom. The forward pump had a power of 14 mW, and the backward beam had a power of 8 mW. Figures 3a and 3b show the power dependency of the right and left circularly polarized components of the conjugate, C as a function of the Ti:Sapphire frequency. As expected, the conjugate is almost fully right circularly polarized. Another important feature is that the Zeeman induced Λ systems method produced a strong conjugate at these low pump powers. Furthermore, since the level of signal power is saturating the power transfer from the pump beams, the reflectivity can be as high as three for this input pump power. By increasing pump intensities by a factor of two, we have observed reflectivities as high as 20.

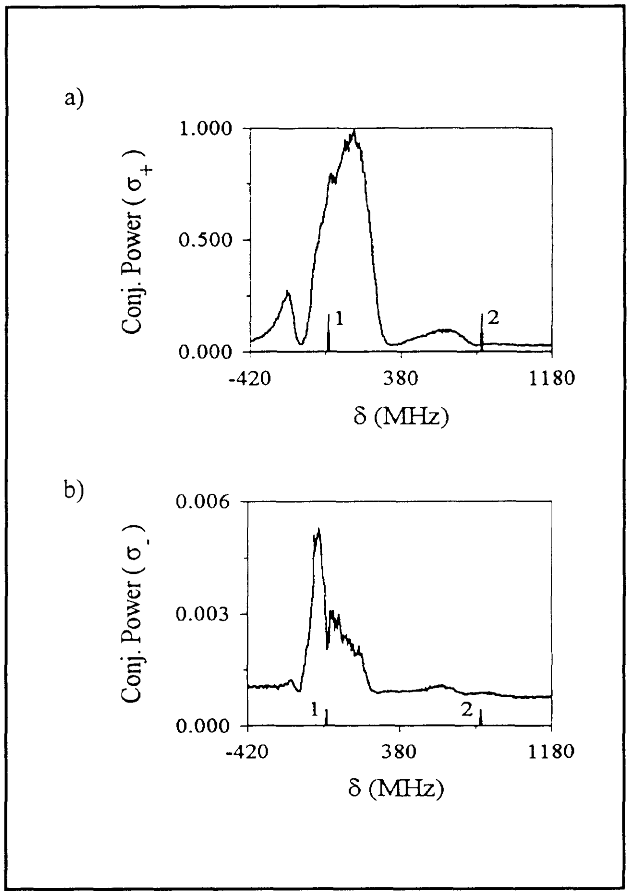

Figure 3. Dependence of the phase conjugation process on the laser frequency: (a) right circularly polarized component of conjugate, and (b) left circularly polarized component of conjugate.

Figure 4a shows the response of the conjugate, C, when we scan the magnetic field (e.g., Δ_z). Since the Zeeman shift for small fields is well understood, we can find the FWHM for this shift (2.4 MHz). This subnatural linewidth (Γ = 5.89 MHz) is quite consistent with our proposed mechanism. By examining the system (see figure 1), one can see that a change in the magnetic field is equivalent to a change in the signal detuning. As a self-consistency check we can also detune the signal beam via the two AOMs. Figure 4b demonstrates the conjugate power, C, as a function of signal detuning. Here we find a FWHM of 3.4 MHz, which we feel is consistent with the previous method, given the large margin of error due to significant changes in the AO efficiency as a function of detuning. If we assume that the linewidth is primarily due to the optical pumping rate, we can calculate a response time of 66 nsec.

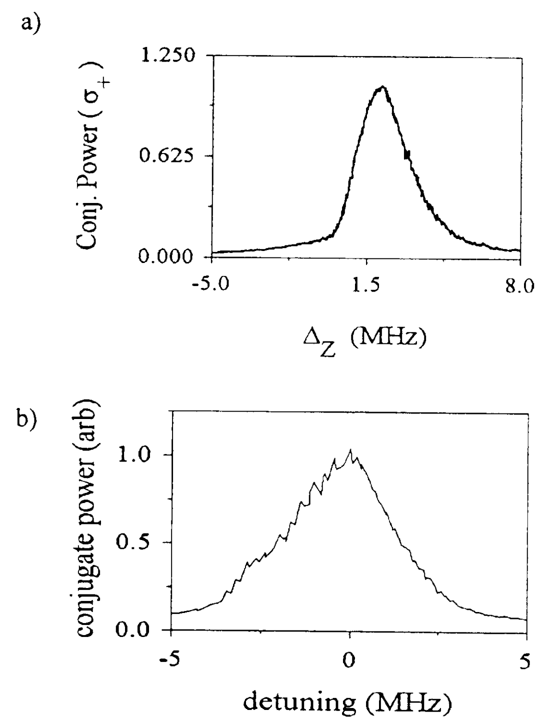

Figure 4. Dependence of the conjugate power on the two-photon detuning for the foward pump and the probe beams: (a) conjugate power as a function of explicit two-photon detuning, with a subnatural linewidth, characteristic of the coherent population trapping process, and (b) conjugate power as a function of the Zeeman detuning between the two lower state sublevels, again showing subnatural linewidth.

Finally, we examined the conjugate's dependence on the backward pump polarization. By inserting a $\lambda/2$ plate between the beam-splitting cube (the first cube the backward beam sees) and the $\lambda/4$ plate, we can cycle through all polarizations. Figure 5 shows the result of this test. When the $\lambda/2$ plate is rotated 45 degrees in either direction, the backward beam is changed from σ_- polarization to σ_+ polarization. Thus, as our model would predict, the conjugate beam disappears when the polarization is incorrect.

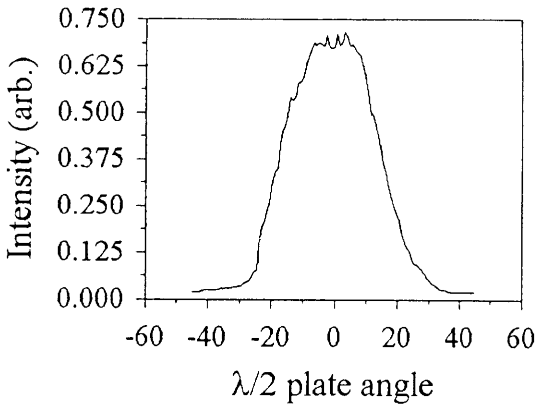

Figure 5. Dependence of the conjugate power on the polarization of the backward pump. The sinsoidal variation is as expected from the model of the process presented here.

In summary, we have developed a new technique of four-wave mixing in vapors using a Zeeman induced Λ system. For one particular transition, (^{87}Rb $5^2S_{1/2}$ F = 2 → $5^2P_{1/2}$ F = 1), we found a conjugate with a reflectivity of 2.5, a reaction time on the order of 66 nsec, at low pump intensities (14 mW for the forward pump and 8 mW for the backward pump with both beams having a FWHM of 1.0 mm). By increasing the intensities by a factor of 20, we have observed reflectivies as high as 20. It should be noted that although we used a Ti:Sapphire laser to generate the beams, diode lasers could provide the necessary pump power.

Currently, we are working on using this conjugator to observe squeezing of quantum noise with application to faint image detection.

1.2 Turbulence Aberration Correction with High-Speed High-Gain Optical Phase Conjugation in Sodium Vapor

Sponsor

U.S. Air Force - Electronic Systems Division
Contract F19628-92-K-0013

Adaptive optic systems can correct for turbulence aberrations in the atmospheric propagation regime, at speeds up to 300 Hz. However, in the aero-optical regime of turbulence, the required bandwidth[7] is up to 100 kHz. It is well known[8] that phase aberrations induced by turbulence can be corrected by optical phase conjugation utilizing nonlinear optical materials. Fast response can be achieved by using photorefractive media, but this requires high-peak-power pump beams available only from pulsed lasers.[9] In this paper, we demonstrate the use of cw lasers with low intensities on the order of 5 W/cm^2 to perform high-speed spatiotemporal aberration correction and still achieve a high-phase conjugate gain. We demonstrate experimentally a temporal aberration correction factor of 7.8 at a frequency of 18 kHz with a conjugate gain of 32. This opens new possibilities in the application of optical phase conjugation to turbulence aberration correction, for example, in phase conjugate resonators.

Previously, we reported[10] a high-conjugate gain with a response faster than 1 ms employing Gaussian beams and low pump intensities of ~ 1 W/cm^2. This was achieved in an externally pumped FWM configuration utilizing the mechanism of coherent population trapping (CPT) in sodium (Na) vapor.[11] Such low-pump intensities could be used because the optical nonlinearity saturates at an intensity below that needed to saturate the optical transition, due to CPT being an optical pumping process. Recently, we have shown that this performance does not degrade in the presence of large angle aberrations caused by a turbulent jet flow.

The FWM configuration for aberration in Na vapor is shown schematically in figure 6. Two different ring dye lasers tuned approximately to the D1 transition are used to produce the forward, F, and backward, B, pumps. The probe beam P is derived from F by using an acousto-optic modulator (AOM) configured for upshifting the frequency of F by 1.772 GHz, which is equal to the ground-state hyperfine transition frequency of Na. This method of using an AOM to obtain a probe beam upshifted from F ensures that the laser jitters of F and P are correlated as required for efficient CPT.[12] In this FWM configuration,[13] the conjugate beam, C, is produced when B scatters off the grating formed by F and P. The probe beam P makes an angle of ~5 mrad with the pump F in the vertical plane. To avoid laser feedback, the counter-propagating pump beams F and B are misaligned by ~1 mrad in the horizontal plane. The typical optical intensities of the collimated F and B beams are ~4.9 W/cm^2 while that of the weaker P beam is ~1.3 mW/cm^2. The typical FWHM spot sizes of the collimated F and B beams are about 1.2 and 1.3 mm respectively, and that of the probe beam ~0.7 mm at the center of the Na cell. The F and B pumps have an identical linear polarization. The P beam is cross-polarized relative to the F and B beams and steered into the cell using a polarizing beam splitter (PBS), as shown in figure 6. The Na vapor cell is a heat-pipe oven operated at ~215 degress C and an ambient background pressure of ~13 mTorr, and is magnetically shielded to better than 100 mG. No buffer gas was added to the Na vapor cell.

As shown in figure 6, the initially collimated probe beam P is passed through an unheated turbulent helium gas jet in air. A lens (f = 17.5 cm) arranged in an approximate 4f configuration images this jet with a slight (9 percent) reduction into the active region of the cell. Hot-wire oscillograms recorded for a helium jet and an air jet reported in Riva et al.[14] show that the phase aberrations in the helium jet arise from the refractive index difference between helium and air. The turbulent jet is produced by forcing helium gas at room temperature through a rectangular nozzle (4 mm X 0.125 mm), aligned with the 4 mm side along the path of P (see the inset in figure 1). The nozzle is located about 2

---

[7] See, for example, *Optical Phase Conjugation*, ed. R.A. Fisher, (New York: Academic Press, 1983).

[8] R.J. Hugo and E.J. Jumper, *Appl. Opt.* 35: 4436 (1996).

[9] See, for example, B. Monson, G.J. Salamo, A.G. Mott, M.J. Miller, E.J. Sharp, W.W. Clark III, G.L. Wood, and R.R. Neurgaonkar, *Opt. Lett.* 15: 12 (1990).

[10] P.R. Hemmer, D.P. Katz, J. Donoghue, M. Cronin-Golomb, M.S. Shahriar, and P. Kumar, *Opt. Lett.* 20: 982 (1995).

[11] P.R. Hemmer, D.P. Katz, J. Donoghue, M. Cronin-Golomb, M.S. Shahriar, and P. Kumar, *Opt. Lett.* 20: 982 (1995); G. Alzetta, A. Gozzini, L. Moi, and G. Orriols, *Nuovo Cimento B* 36: 5 (1976); H.R. Gray, R.M. Whitley, and C.R. Stroud, *Opt. Lett.* 3: 218 (1978); P.M. Radmore and P.L. Knight, *J. Phys. B* 15: 3405 (1982); J. Donoghue, M. Cronin-Golomb, J.S. Kane, and P.R. Hemmer, *Opt. Lett.* 16: 1313 (1991).

[12] J.E. Thomas, P.R. Hemmer, S. Ezekiel, C.C. Leiby, Jr., R.H. Picard, and C.R. Willis, *Phys. Rev. Lett.* 48: 867 (1982).

[13] P.R. Hemmer, D.P. Katz, J. Donoghue, M. Cronin-Golomb, M.S. Shahriar, and P. Kumar, *Opt. Lett.* 20: 982 (1995).

[14] R. Riva, G. Binder, S. Tardu, and M. Favre-Marinet, in *Turbulence and Coherent Structures,* eds. O. Metais and M. Lesieur (Dordrecht: Kluwer, 1991).

mm below the probe beam path, at a distance of ~70 cm from the center of the Na cell. The average helium flow velocity at the nozzle exit was estimated from the volume flow rate of 11 CFH and the area of the nozzle (0.5 mm^2) to be about 170 meters/sec.

In order to facilitate quantitative measurements of the temporal aberrations induced by the turbulent jet, the nozzle was driven by a PZT transducer at a resonance frequency of 17.8 kHz. It is known[15] that eddy structures in the growth and mixing of turbulent jets are sensitive to harmonic forcing and that such controlled excitation can accentuate the coherent structures and localize their interactions, thus providing an easy way of studying them.[16] Resonance at a higher frequency of 45 kHz (and up to 75 kHz) was observed, but the output signal was limited by the appearance of strong subharmonics of the PZT drive frequency. The mechanism of the generation of subharmonics specific to our nozzle and jet was not investigated, but can be probably related to eddy behavior reported by others.[16] However, for the flow velocities utilized here, the resonance at 17.8 kHz provided a sinusoidal photodetector signal at the fundamental frequency permitting a more accurate determination of the aberration correction factor.

As shown in figure 6, the conjugate beam, C, is picked off first at the beamsplitter BS1 to be viewed through a CCD camera, and secondly, at BS2 to be detected simultaneously at the photodetector, D, for power gain measurements and at a pinhole-detector assembly, PD. The temporal aberration effects of turbulence are measured with PD. The PD assembly consists of a pinhole (0.2 mm diameter) placed 1 mm in front of a photodetector and is ~164 cm distant from the nozzle center. For the measurement of probe aberration, the P beam made a single-pass through the helium jet and was reflected onto PD and the CCD using a removable mirror M. The position of the pinhole of PD is adjusted for maximum ac signal amplitude at the forcing frequency. The ratio of this peak-to-peak ac voltage to the maximum voltage level is termed the modulation depth. This is chosen as the experimental measure of the temporal aberration at the forcing frequency because it compensates for the difference in the intensities of the conjugate and probe beams.

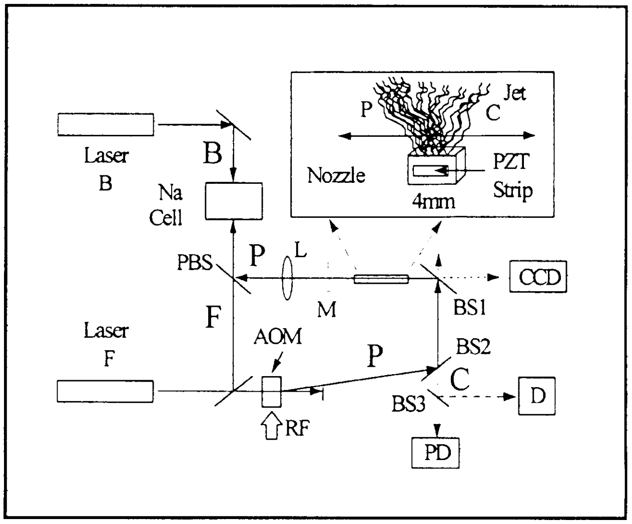

Figure 6. Schematic diagram of the experimental set-up for turbulence aberration correction using FWM based Na vapor phase conjugate mirror.

The plots of the instantaneous output voltage from PD are displayed in figure 7 for the probe and conjugate beams. The trace in figure 7a shows the electrical input signal at 17.8 kHz applied to the PZT strip on the jet nozzle. The trace in figure 7b shows the optical effect of turbulence on P after a single pass through the helium jet. The trace in figure 7c shows the optical effect of the turbulence on C that has very closely retraced the path of P, traveling back through the turbulent flow. From this data, the signal modulation depth, as defined earlier, in the probe beam is estimated at 63 percent while that for the conjugate beam is estimated at 8 percent, thus demonstrating that turbulence aberrations in the conjugate beam are corrected by a factor of 7.8. In figure 7c, any stray light reaching PD from B passing through the PBS and L (see figure 6) is less than 1 percent of the peak signal from C.

---

[15] S.C. Crow and F.H. Champagne, *J. Fluid Mech.* 48: 547 (1971).

[16] K.M.F. Hussain and K.M.B.Q. Zaman, in *Structure and Mechanisms of Turbulence I, Proceedings of the Symposium on Turbulence*, ed. H. Fiedler (Berlin: Springer-Verlag, 1978) p. 31.

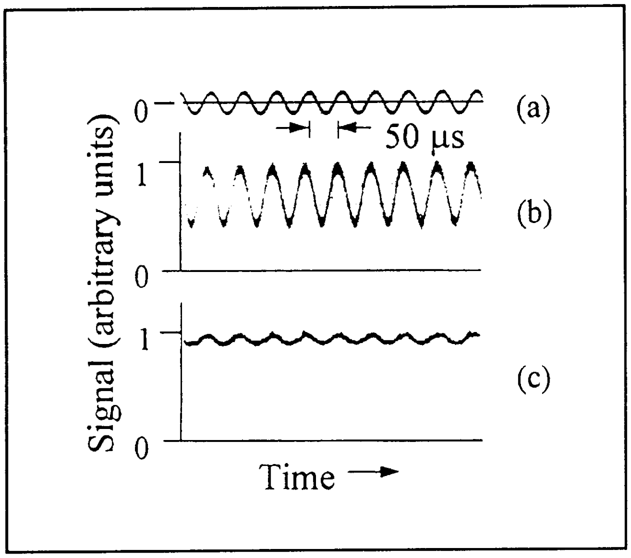

Figure 7. Temporal aberration correction: (a) electrical input signal at 17.82 kHz applied to the PZT strip, (b) aberrated probe signal at PD after a single pass through the helium jet, and (c) corrected conjugate signal at PD after retraversal through the jet.

Spatial aberration correction is demonstrated in figure 8 through images captured with the CCD camera. The profile of C after retraversing the probe path and passing through the turbulent helium jet is shown in the 2-d contour plot and 1-d line trace in figure 8a. As seen, a well-corrected, diffraction-limited nearly-circular spot is observed. Here the conjugate gain is ~32. This is to be compared to the profile of P in figure 8b after a single pass through the turbulent jet. Note the large aberration and the distinct far-field flow pattern. The extent and geometry of the flow pattern was dependent on the drive frequency, flow velocity, distance of the nozzle exit plane from the probe beam, and jet alignment with respect to the probe beam. To determine how the conjugate gain is affected by the aberration, figure 8c shows the profile of C when the helium flow is cut off. Here the conjugate gain is ~45 which shows that the aberration did not excessively degrade the conjugate performance. Finally, figure 8d shows the profile of P without flow.

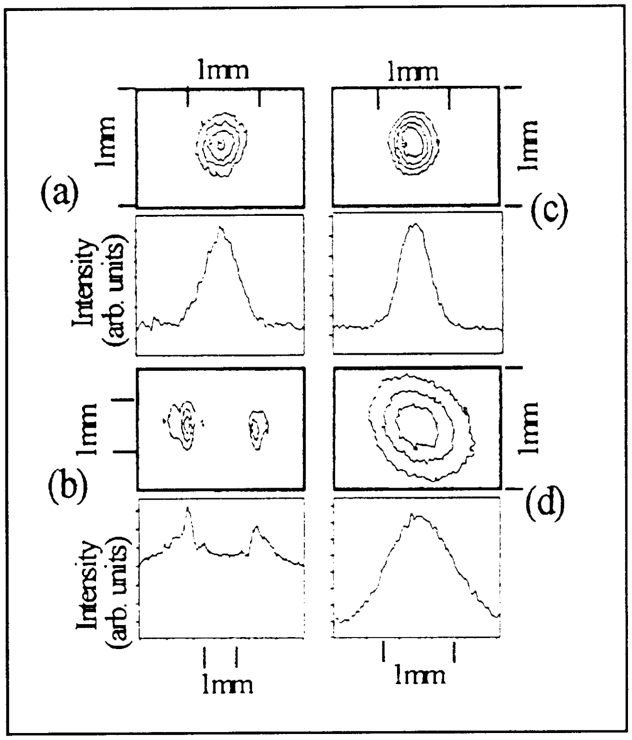

Figure 8. Spatial aberration correction: 2-d contours (upper plots) and 1-d line traces (lower plots) of the spatial intensity distribution of (a) the conjugate beam with helium flow ON, (b) the probe beam with helium flow ON, (c) the conjugate beam with helium flow OFF, and (d) the probe beam with helium flow OFF. Contours are drawn in (a) and (c) at 80 percent, 60 percent, 40 percent, and 20 percent of the peak intensity, whereas in (b) and (d) at 75 percent, 50 percent, and 25 percent of the peak intensity.

Figure 9a shows the conjugate gain as a function of the frequency, ω_F, of the laser F in the presence of helium flow. It is to be noted that the frequency of the probe beam is also simultaneously scanned as P is simply upshifted from F by using the AOM. Figure 9b shows the phase conjugate gain as a function of the frequency, ω_B, of the laser B. The peak conjugate gain occured when F and B (P and C) were tuned as shown in figure 9c. The FWHM of the gain peaks in figure 9a and 9b were measured to be 118 MHz and 127 MHz respectively. It should be noted that the Doppler width of Na vapor at 215 degrees C is about 1 GHz, and the hyperfine separation between F'=1 and F'=2 is 190 MHz. A similar conjugate gain of ~26 was obtained when F was blue-detuned 126 MHz from the F=2 to F'=2 transition and B was red-detuned 190 MHz from the F=1 to F'=1 transition.

To confirm that the gain mechanism in these measurements was indeed CPT, the two-photon resonance width was determined by scanning the frequency, ω_{rf}, of the AOM and measuring the linewidth of the gain. This is shown in figure 9d. As seen, the FWHM of the gain is 2 MHz, which is smaller than the 10 MHz natural linewidth of Na. This subnatural rf frequency linewidth provides evidence of CPT.[17]

An estimate of the phase conjugate response time can be obtained from the reciprocal of the linewidth, which from figure 9d was found to be 79 ns. This is much faster than the forcing frequency of 17.8 kHz set by the particular characteristics of the PZT-nozzle assembly, and hence the temporal aberration correction of 7.8 as shown in figure 7 should not be limited by the phase conjugate response time. To explain lack of complete correction, we note that earlier reports[18] have shown that pump misalignments can greatly reduce the amount of aberration correction otherwise possible in an ideally counter-propagating configuration. As already mentioned, the F and B beams were slightly misaligned in our experimental set-up to avoid instabilities arising from laser feedback. However, this feedback problem can be overcome by using optical isolators.

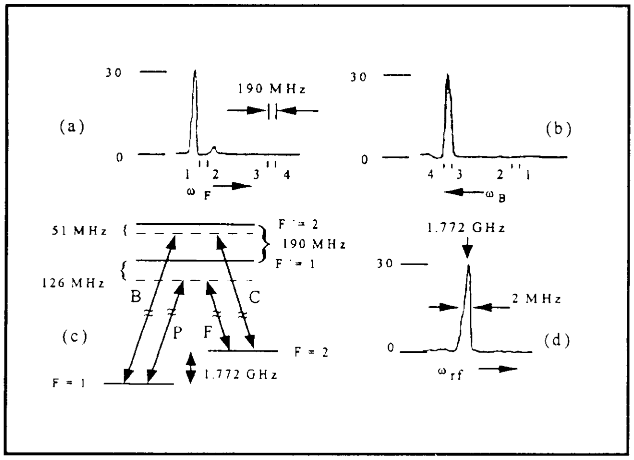

Figure 9. The conjugate gain as a function of (a) the frequency ω_F, (b) the frequency ω_B, and (d) the frequency, ω_{rf}. The energy level diagram for the double-L transitions proposed are shown in (c). The numbers 1 through 4 in (a) and (b) correspond to 1: F=2 to F'=1; 2: F=2 to F'=2; 3: F=1 to F'=1, and 4: F=1 to F'=2.

In summary, high speed aero-optical turbulence aberrations at a frequency of 18 kHz have been corrected for by a factor of 7.8 with a high gain of 32. This is accomplished utilizing CPT-based phase conjugation in Na vapor in an FWM configuration.

1.3 Enhanced Nondegenerate Four-wave-mixing due to Electromagnetically Induced Transparency in a Spectral Hole Burning Crystal for Five-Dimensional Optical Data Storage

Sponsor

U.S. Air Force - Electronic Systems Division
Contract F30602-95-C-0088
Contract F49620-96-1-0395

We have demonstrated suppressed absorption and enhanced nondegenerate four-wave mixing (NDFWM) based on electromagnetically induced transparency (EIT) in a spectral hole-burning crystal with a cw laser at 6 K. Previous observations of EIT have been restricted to vapors and atomic beams.[19] However, in these materials the diffusion of atoms is a major problem and limits applications, especially when working with images. Spectral hole-burning solid materials have many similarities to vapors and beams in that the optical transitions are between energy levels of isolated ions, but have the advantages of permanent optical pumping (storage capability) and absence of diffusion. This opens the door to numerous additional applications

---

[17] K.M.F. Hussain and K.M.B.Q. Zaman, in *Structure and Mechanisms of Turbulence I, Proceedings of the Symposium on Turbulence*, ed. H. Fiedler (Berlin: Springer-Verlag, 1978), p. 31; G. Alzetta, A. Gozzini, L. Moi, and G. Orriols, *Nuovo Cimento B* 36: 5 (1976); H.R. Gray, R.M. Whitley, and C.R. Stroud, *Opt. Lett.* 3: 218 (1978); P.M. Radmore and P.L. Knight, *J. Phys. B* 15: 3405 (1982); J. Donoghue, M. Cronin-Golomb, J.S. Kane, and P.R. Hemmer, *Opt. Lett.* 16: 1313 (1991).

[18] See for example, *Optical Phase Conjugation*, ed. R.A. Fischer (New York: Academic Press, 1983).

[19] K.J. Boller, A. Imamoglu, and S.E. Harris, *Phys. Rev. Lett.* 66: 2593 (1991); J.E. Field, K.H. Hann, and S.E. Harris, *Phys. Rev. Lett.* 67: 3062 (1991); M. Xiao, Y. Li, S. Jin, and J. Gea-Banacloche, *Phys. Rev. Lett.* 74: 666 (1995); J.E. Thomas, P.R. Hemmer, S. Ezekiel, C.C. Leiby, Jr., R.H. Picard, and C.R. Willis, *Phys. Rev. Lett.* 48: 867 (1982).

to spectroscopy,[20] image processing,[21] real-time holography,[22] and optical memory.[23]

Atom-field interactions in three-level systems have been studied extensively in the last several years. After the first observation of coherent population trapping (CPT) in a sodium beam,[24] many potential applications have been explored. The most recent applications of interest include nonlinear optical processes for frequency conversion,[25] lasers without population inversion (LWI),[26] Raman excited spin echo data storage,[27] and high-gain, low-intensity optical phase conjugation.[28] In the area of frequency conversion, Harris et al. proposed the creation of nonlinear media with resonantly enhanced nonlinear susceptibilities and at the same time reduced absorption at the resonant transition frequency owing to EIT.[29] Recent experiments have shown enhanced second harmonic generation[30] and third harmonic generation[31] using EIT. In the area of LWI, there has been an experimental demonstration in Rb vapor,[32] and there is current interest in finding suitable solid materials. For Raman excited spin echoes, a sodium atomic beam experiment has been performed to verify the basic physics. This process is now being considered for high temperature persistent spectral hole burning memories, because spin coherence survives longer than optical coherence at high temperature.[33] In the area of optical phase conjugation via four-wave mixing, Hemmer et al. recently observed high gain phase conjugation in sodium vapor using CPT.[34] Li et al. also observed the enhancement of NDFWM as a result of EIT effect in a L-type three-level system of Rb.[35]

Figure 10 shows the energy level diagram of Pr^{3+} doped Y_2SiO_5(Pr:YSO) for NDFWM. Our system consists of 0.05 at. percent Pr doped YSO in which Pr ions act like an inhomogeneously broadened six-level atomic system. Pr:YSO is known as a good material for optical spectral hole-burning data-storage because of its big ratio of inhomogeneous to homogeneous widths and long optical pumping lifetime. For this work, the relevant optical transition is $^3H_4 \rightarrow {}^1D_2$ which has a frequency of 605.7 nm at site 1. The optical T_1 and T_2 are 164 μs and

---

[20] D.G. Steel and J.F. Lam, *Phys. Rev. Lett.* 43: 1588 (1979); D. Zimdars, A. Tokmakoff, S. Chen, S.R. Greenfield, and M.D. Fayer, *Phys. Rev. Lett.* 70: 2718 (1993).

[21] E.Y. Xu, S. Kroll, D.L. Huestis, R. Kachru, and M.K. Kim, *Opt. Lett.* 15: 562 (1990).

[22] F. Ito and K. Kitayama, *Opt. Lett.* 17: 1152 (1992).

[23] M.K. Kim and R. Kachru, *Opt. Lett.* 14: 423 (1989).

[24] G. Alzetta, A. Gozzini, L. Moi, and G. Orriols, *Nuovo Cimento* B 36: 5 (1976); H.R. Gray, R.M. Whitley, and C.R. Stroud, *Opt. Lett.* 3: 218 (1978).

[25] K. Hakuta, L. Marmet, and B.P. Stoicheff, *Phys. Rev. Lett.* 66: 596 (1991); Phys. Rev. Lett. 45: 5152 (1992); G.Z. Zhang, K. Hakuta, and B.P. Stoicheff, *Phys. Rev. Lett.* 71: 3099 (1993); S.P. Tewari and G.S. Agarwal, *Phys. Rev. Lett.* 56: 1811 (1986); R.P. Blacewicz, M.G. Payne, W.R. Garrett, and J.C. Miler, *Phys. Rev.* A 34: 5171 (1986).

[26] O.A. Kocharovskaya and Y.I. Khanin, *JETP Lett.* 48: 630 (1988); S.E. Harris, *Phys. Rev. Lett.* 62: 1033 (1989); M.D. Scully and S.Y. Zhu, *Phys. Rev. Lett.* 62: 2813 (1989).

[27] P.R. Hemmer, M.S. Shahriar, B.S. Ham, M.K. Kim, and Y. Rozhdestvensky, *Mol. Cryst. Liq. Cryst.* 291: 287 (1996).

[28] P.R. Hemmer, D.P. Katz, J. Donoghue, M. Cronin-Golomb, M.S. Shahriar, and P. Kumar, *Opt. Lett.* 20: 982 (1995).

[29] S.E. Harris, J.E. Field, and A. Imamoglu, *Phys. Rev. Lett.* 64: 1107 (1990).

[30] K. Hakuta, L. Marmet, and B.P. Stoicheff, *Phys. Rev. Lett.* 66: 596 (1991); *Phys. Rev. Lett.* 45: 5152 (1992); G.Z. Zhang, K. Hakuta, and B.P. Stoicheff, *Phys. Rev. Lett.* 71: 3099 (1993).

[31] S.P. Tewari and G.S. Agarwal, *Phys. Rev. Lett.* 56: 1811 (1986); R.P. Blacewicz, M.G. Payne, W.R. Garrett, and J.C. Miler, *Phys. Rev.* A 34: 5171 (1986).

[32] A.S. Zibov, M.D. Lukin, D.E. Nikonov, L. Hollberg, M.O. Scully, V.L. Velicharsky, and H.G. Robinson, *Phys. Rev. Lett.* 75: 1499 (1995).

[33] P.R. Hemmer, S.M. Shahriar, Z. Cheng, J. Kiersted, and M.K. Kim, *Opt. Lett.* 65: 1865 (1994).

[34] P.R. Hemmer, D.P. Katz, J. Donoghue, M. Cronin-Golomb, M.S. Shahriar, and P. Kumar, *Opt. Lett.* 20: 982 (1995).

[35] Y.Q. Li and M. Xiao, *Opt. Lett.* 21: 1064 (1996).

477 μs, respectively at 1.4 degrees K,[36] and the optical inhomogeneous width is about 4 GHz. The ground and excited states each have three Kramer's doublets.[37] The transition frequency of the ground state Kramer's doublets are 10.2 MHz and 17.3 MHz. The transverse relaxation time T_2 between Kramer's doublets has not been directly measured, but the population relaxation time T_1 is as long as several minutes. The inhomogeneous widths of transitions between ground-state Kramer's doublets measured by optically detected nuclear magnetic resonance (ODNMR) are known to be less than 80 kHz.17 For the 10.2 MHz transition, we measured an inhomogeneous linewidth of 40 kHz. In general, EIT implies the use of high optical density material. Pr:YSO is a good material for such studies because it can have a high optical density (neglecting optical pump effects). Measured absorption coefficients[37] are as large as 10 cm^{-1}.

Laser fields ω_2 and ω_3 in figure 10 can be viewed as write beams, which create a ground state coherence via EIT. Laser field ω_1 then acts as a read beam to generate a beam ω_4, while a laser field ω_R acts as a repump beam. As shown, the write beam ω_3 is on resonance with the transition $^3H_4(\pm3/2) \rightarrow {}^1D_2\ (\pm5/2)$ while the write beam ω_2 is scanned across the resonance frequency of $^3H_4(\pm5/2) \rightarrow {}^1D_2\ (\pm5/2)$ The read beam ω_1 is blue detuned from the write beam by a frequency of Δ = 100 kHz which is larger than the inhomogeneous width of transitions between Kramer's doublets. The generated beam ω_4 must satisfy the phase-matching condition of $\vec{k}_4 = \vec{k}_1 + \vec{k}_2 - \vec{k}_3$. Here it should be noted that figure 10 applies to only a small subset of Pr-ions. Due to the large inhomogeneous broadening, each laser field can pump other transitions in the manifold for a subset of Pr-ions having the appropriate transition frequency. However, due to optical pumping, only the subset of Pr-ions shown in figure 10 is repumped, and therefore, for cw excitation, all the signals come from this system.

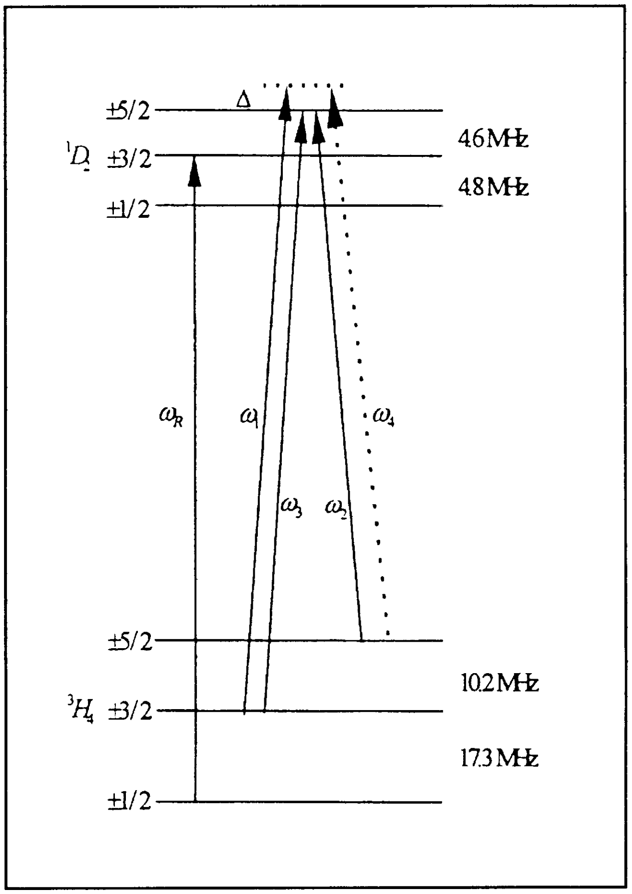

Figure 10. The energy level diagram of Pr:YSO for four-wave mixing.

Figure 11 shows the schematic experimental setup for observing EIT and NDFWM in Pr:YSO. We use a frequency stabilized Coherent ring dye laser 699 pumped by a Spectra Physics argon ion laser. The laser is continuous wave, and its estimated linewidth is 3 MHz. We use acousto-optic modulators (AO) driven by frequency synthesizers to make four different coherent laser beams as shown. To match figure 10, the write beams ω_2 and ω_3 are upshifted 54.8 MHz and 65.0 MHz from the laser frequency by AO-2 and AO-3, respectively. The read beam ω_1 and the repump beam ω_R are upshifted 65.1 MHz and 77.8 MHz by AO-1 and AO-R, respectively. To escape from any possible contribution of coherent interaction between the repump and the two-photon transitions, the repump transition is chosen as shown in figure 10. These four laser beams are focused into the sample by a 40 cm focal length lens. The beam diameters ($1/e^2$) are about 150 mm in the crystal. Each applied

---

[36] R.W. Equall, R.L. Cone, and R.M. Macfarlane, *Phys. Rev. B* 52: 3963 (1995).

[37] K. Holliday, M. Croci, E. Vauthey, and U.P. Wild, *Phys. Rev. B* 47: 14741 (1993).

laser intensity of ω_1, ω_2, ω_3, and ω_R is about 20, 40, 60, and 60 W/cm^2, respectively. The angle between the two write beams is about 70 mrad. The hole-burning crystal Pr:YSO is inside the helium cryostat. We keep the temperature at 6 degrees K. If the temperature is over 10 degrees K, no spectral hole-burning phenomenon is observed. The size of the crystal is 3 mm in diameter and 10 mm in length. Its optical B-axis is unknown, and the absorption is very polarization-sensitive. Under these conditions, we measure that the maximum absorption of laser beam ω_2 is 85 percent which is limited by the strength of the repump beam.

To measure the effective optical linewidth of the repumped atom source, the laser intensities are reduced by a factor of 10, and the read beam ω_1 is blocked. As already mentioned, the laser beams ω_2 and ω_3 burn spectral holes on ground states (±3/2 and ±5/2), while the repump beam ω_R refills burned holes, thereby serving as an effective narrowband source of atoms. The absorption width seen as ω_2 is scanned depends on both the homogeneous width of the optical transition and on the applied laser field linewidth, which can be broadened by laser jitter. In our case, the laser linewidth dominates because it is much broader than the optical homogeneous width. Figure 12 shows the absorption spectrum of the beam ω_2 with beams ω_3 and ω_R tuned near the center of the 4 GHz inhomogeneously broadened absorption profile of Pr:YSO. No two-photon transition is seen because of insufficient laser intensity. The full width at half maximum (FWHM) of the absorption spectrum is about 3.5 MHz, which is similar to the estimated laser linewidth based on laser jitter observed with a Fabry-Perot spectrum analyzer. The absorption curve disappears when the repump field ω_R is blocked as expected. The noise seen on the data is due to the combined effects of laser jitter and the spectral hole-burning process.

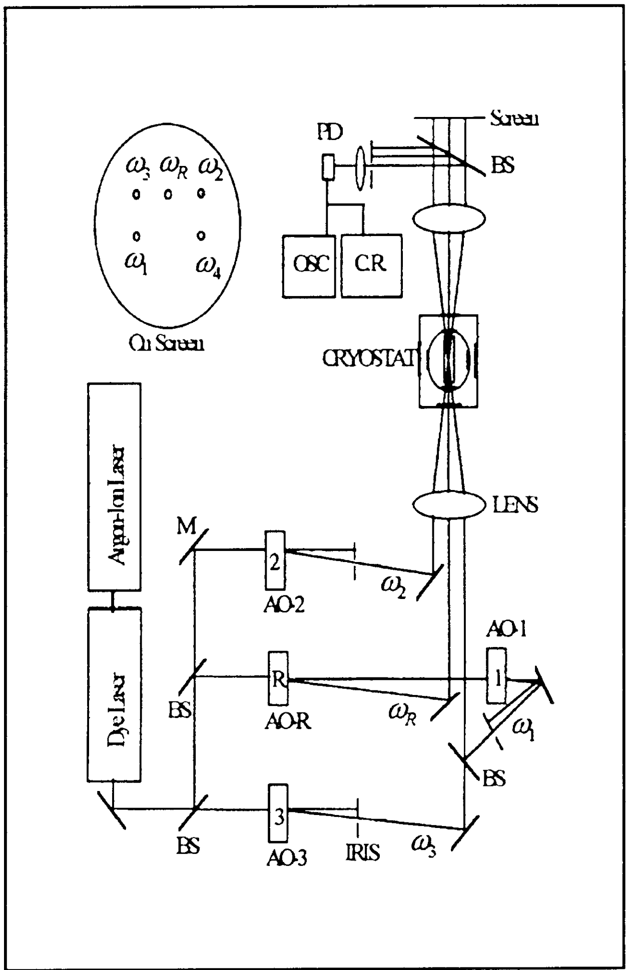

Figure 11. The schemetic diagram of non-degenerate four-wave mixing in Pr:YSO; AO, Acousto-optic modulator; BS, Beam splitter; C.R., Chart recorder; M, Mirror; OSC, Oscilloscope; PD, Photo diode.

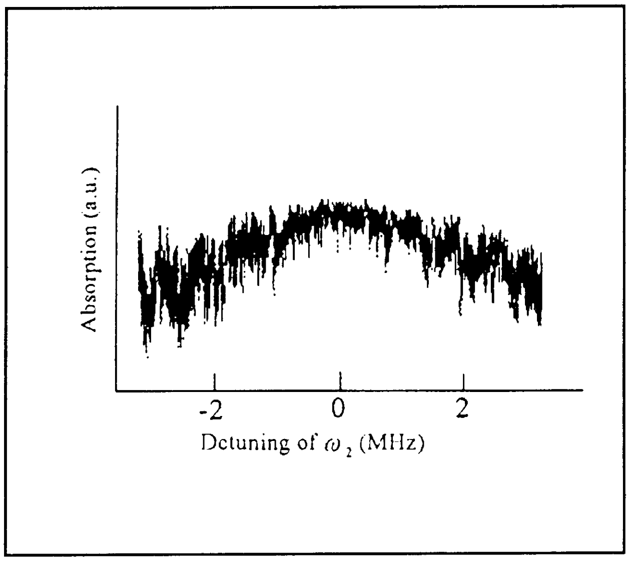

Figure 12. Absorption spectrum of beam ω_2 with weak beams ω_3 and ω_R.

To demonstrate EIT explicitly, we increase the laser intensities of ω_3 and ω_R, and again scan the weak laser beam ω_2 across the two-photon resonance frequency, keeping ω_3 and ω_R fixed. In figure 13a, we demonstrate that the absorption of ω_2 is reduced at two photon resonance frequency of ω_2 and ω_3. The scan range is reduced because the width of suppressed absorption by EIT is much narrower than the single photon absorption spectrum in figure 12. The measured absorption is reduced from 85 percent to 70 percent. The FWHM of the reduced absorption is 60 kHz, which is much narrower than the laser linewidth and comparable to the spin state inhomogeneous linewidth of $^3H_4(\pm3/2)\leftrightarrow{}^3H_4(\pm5/2)$, which is 40 kHz. This insensitivity to laser jitters is the signature of two-photon transitions responsible for EIT. Thus, the reduced absorption is due to the EIT effect.

For the four-wave mixing experiment, we add the read beam ω_1, which is 100 kHz blue-detuned from the write beam ω_3 (see figure 10). Even though this detuning is much smaller than the laser jitter, ω_1 and ω_3 are never degenerate, because the fields are generated with AOs from a single laser (see figure 11). The alignments of laser beams ω_1, ω_2, and ω_3 satisfy Bragg condition for the generation of ω_4 at the position indicated in the inset in figure 11 which shows spatial positions of four laser beams on the screen. Figure 13b shows the intensity of the diffracted signal ω_4 as a function of the detuning of ω_2 from the two photon resonant transition. The diffracted signal ω_4 is enhanced greatly as the write beam ω_2 is tuned through two photon resonance, and its FWHM is 40 kHz. The diffraction efficiency, i.e., intensity ratio of ω_4 to ω_1 is about 1 percent. Again, sublaser jitter linewidth is the evidence of EIT. Therefore the enhancement of nonlinear generation in NDFWM is due to the ground state coherence produced by EIT.

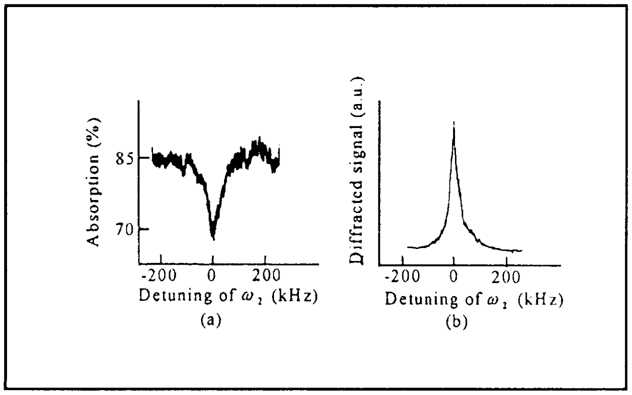

Figure 13. (a) Absorption spectrum of beam ω_2 with strong beams ω_3 and ω_R. (b) NDFWM generation in inhomogeneously broadened spectral hole-burning crystal Pr:YSO at 6 degrees K.

In summary, we have observed electromagnetically induced transparency (EIT) in an inhomogeneously broadened spectral hole-burning system of Pr:YSO at 6 degrees K. We showed the simultaneous reduction of absorption and enhancement of four wave mixing. This material is an attractive alternative to vapor because it opens the possibilities of pursuing EIT applications such as high-resolution nonlinear optical image processing. Most importantly, this represents a significant step in our efforts to use the two-photon Raman interaction to perform ultra-high-density, five-dimensional optical data storage.

1.4 Long-Term Optical Data Storage in Three and Four Dimensions Using Thick Holograms

Sponsors

U.S. Ballistic Missile Defense Organization
  Grant NG0921-94-C-0101
U.S. Air Force - Office of Scientific Research/
  AASERT
  Grant F49620-96-1-0308

The five-dimensional data storage scheme discussed above would be useful as a dynamic memory, using optical pulses. On the other hand, many applications require long term data storage. We are pursuing two projects to develop such a memory using thick holograms.

The ability to store a large number of holograms in a single recording material is important for the implementation of optical neural networks, optical interconnects, and holographic computing elements. Recently, a strong effort has been undertaken by several groups to develop high-volume data storage devices using holograms. The storage media used fall under two broad categories: spectrally homogeneous systems, and spectrally inhomogeneous systems.

In the case of spectrally homogeneous systems, any information is encoded only in the spatial structure of the optical fields. As such, the fundamental storage capacity in such a system is limited to ~$V/\lambda 3$, where V is the volume, and λ is the wavelength of light. In practice, this limit is difficult to achieve, due primarily to cross-talks. Various techniques, including angle multiplexing, wavelength multiplexing, orthogonal phase encoding, and fractal-space multiplexing, or a combination thereof, have been employed to improve the storage density, although still well below the limit.[38]

In the case of spectrally inhomogeneous systems, the medium contains elements that are not identical, and respond differently to light of a given frequency. In such a medium, the elements within a λ^3 volume have a wide distribution (inhomogeneous width) of responses to the optical frequency. For a given frequency, only a small fraction (homogeneous width) of these atoms get excited, a phenomenon known as spectral hole burning (SHB). This fraction of atoms can store roughly V/λ^3 bits of information. The storage capacity in principle can thus be larger by the number of spectral holes (which can easily approach 1000) given by the ratio of the inhomogeneous width to the homogeneous width. Thus, the SHB storage medium is expected to yield a realizable storage density much higher than spectrally homogeneous holographic media.

1.4.1 Room Temperature Holographic Memory Using Thick Photopolymer

For practical systems of wider use, it is necessary to develop holographic storage systems that will work at room temperature. In principle, a thickness of between 1 and 2 cm provides optimum storage density, due to constraints imposed by optical access requirements. Data storage using holograms of such thickness (1 cm or more) have so far only been performed in photorefractive crystals. However, photopolymeric systems generally have several distinct advantages over photorefractive systems. These include much lower cost, lack of constraint in shape, higher diffraction efficiency, lower refractive index (1.6, compared to 2.2 for typical photorefractives) which implies a larger field of view, simplicity of fixing, and a wide spectral bandwidth (400 to 1500 nm). As such, these material can be used to make a practical disc memory, read by compact semiconductor lasers. For example, the lasers currently used in CD ROMS operate near 800 nm, which is near the peak of the photopolymer sensitivity, but is outside the spectral response curve of Lithium Niobate crystals. However, to date, only thin (100 μm or less) holograms have been successfully used to demonstrate storage in photopolymeric structures.[39] This is due to a host of problems in creating thick holograms of good quality. These problems span issues such as differential shrinkage, non-uniformity of active elements through the substrate, difficulty in embedding materials into substrates, and lack of high quality optical surfaces. As a result, the full potential of holographic data storage in such media is kept limited by the useful thickness. For example, the storage achievable in a 100 mm thick hologram is theoretically two orders of magnitude smaller than what can be achieved in a 1 cm thick hologram. Even within the current limits due to optical accessing architectures, it should be possible to store as much as 150 bits/μm^2 in a 1 cm-thick hologram.

In recent years, many groups around the world have been trying to develop thick photopolymeric holograms suitable for data storage. Arguably, one of the leaders in this pursuit has been the Vavilov State Optical Institute. Very recently, they have succeded in developing novel thick holographic material called photopolymer with diffusion amplification (PDA).[40] This material has an excellent surface quality, causes very low scattering, and has a diffraction efficiency nearing 100 percent, with negligible loss.

This material consists of phenanthraquinone embedded in polymethylmethacrylate (PMMA). This medium uses the novel principle of diffusion amplification of holograms on polymeric recording media. Briefly, photoexposure of this system results in writing of two out-of-phase periodic structures that partially compensate each other. One of these is formed by a concentration distribution of chromatophore groups combined into macromolecules, while the other is formed by free molecules. As a result of diffusion of the free molecules, the corresponding grating degrades, and the resulting grating is amplified *without additional processing*. The surviving grating is stored in macromolecules that do not diffuse.

We are using this material to perform long term, room temperature holographic optical data storage. A typical hologram of PDA is a cylidrical disc with a

---

[38] F.H. Mok, *Opt. Lett.* 18: 915 (1993); S. Tao, D.R. Selviah, and J.E. Midwinter, *Opt. Lett.* 18: 912 (1993); A. Chiou, *Opt. Lett.* 17: 1018 (1992); G. Rakuljic, V. Leyva and A. Yariv, *Opt. Lett.* 17: 1471 (1992); H. Li and D. Psaltis, *Appl. Opt.* 33: 3764 (1994); H. Yu, S. Li, and D. Psaltis, *JOSA A* 12: 1902 (1995).

[39] A. Pu and D. Psaltis, in *Proceeding of OSA Annual Meeting*, Portland, Oregon, 1995 (MEE4); B. Kohler, S. Bernet, A. Renu, and U. Wild, *Opt. Lett.* 18: 2144 (1993).

[40] A.V. Veniaminov, V.F. Goncharov, and A.P. Popov, *Opt. Spectroscopy* (USSR) 70(4): 505-508 (1991), and references therein.

diameter of 10 cm and a thickness of 5 mm (compared to 100 μm for photopolymeric discs currently used). With peristropic and angular multiplexing, such a system will have a net storage capacity of more than 10^{12} bits (>100 Gbytes), estimated conservatively within the currently accepted limits due to optical accessing limitations. We use an Argon laser to write the holograms. The holograms are cured in situ with ease, and without causing any degradation. The read-out system will use single-mode semiconductor lasers at 800 nm, along with other electronic and optical components such as SLMs and CCD cameras.

To start with, we have written holograms in a sample 1.5 mm thick in order to determine the number of holograms that can be superimposed using angular multiplexing.[41] Briefly, the input image and the write beams (both at 488 nm) are both plane waves, used in the transmission configuration. When the hologram is illuminated by a read beam (at 680 nm) at the Bragg angle, the diffracted beam represents the output. Figure 14 illustrates the case where the read beam is diverging, with an angular spread of about 20 mrad. Due to the angular selectivity, however, only a small part of this beam gets diffracted. Figure 14a shows the transmitted beam, with the dark spot in the center corresponding to the diffracted beam shown in figure 14b. In agreement with the theory of thick holograms,[42] the angular selectivity is about 1 mrad.

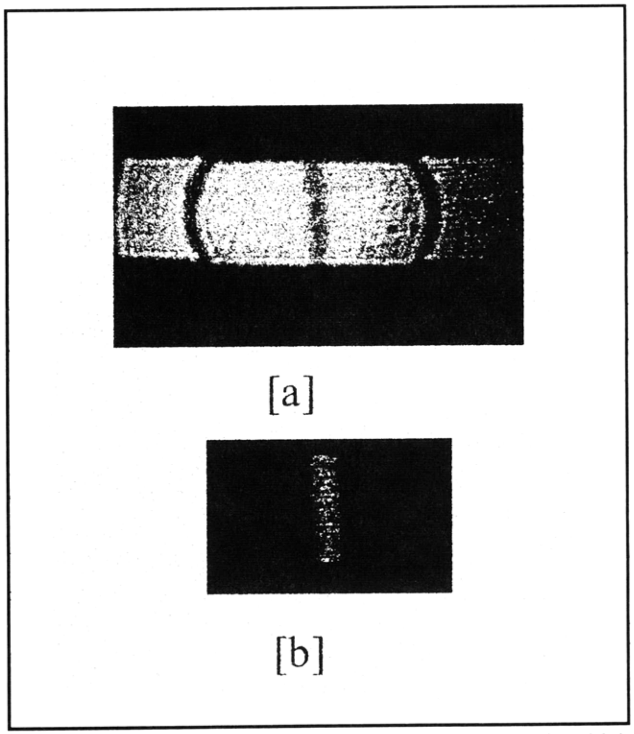

Figure 14. Illustration of the angular selectivity of a thick hologram made of PDA: (a) transmitted profile, and (b) diffracted profile

Figure 15 illustrates the case where the read beam is an image from the Air Force resolution chart. The hologram is placed in the image plane using two lenses, so that the divergence in the image is small. The transmitted spot is shown in figure 15a, and the diffracted spot is shown in figure 15b. As expected, the structure in the vertical direction is reproduce with full fidelity, while any structure in the horizontal direction exceeding the 1 mrad bandwidth is not reproduced in the diffracted output. Note that the output does not suffer from spurious scatterings and image distortions.

We are now working on writing a series of high resolution, digital images using angle multiplexing. The initial goal is to achieve a raw bit error rate (BER) of 10^{-5}, so that with error-correction-codes the real bit error rate can be made as low as 10^{-12}. Once this is achieved, we will work on demonstrating an operational memory disk with a capacity of at least 100 Gbytes, and an access rate of 1 Gbit/sec.

---

[41] J.E. Ludman, J.R. Riccobono, H.J. Caulfield, J.M. Fournier, I.V. Semenova, N.O. Reinhand, P.R. Hemmer, and S.M. Shahriar, in *Proceedings of IS&T Conference*, San Jose, California, February 1995.

[42] H. Kogelnik, *Bell Syst. Tech. J.* 48: 2909 (1969).

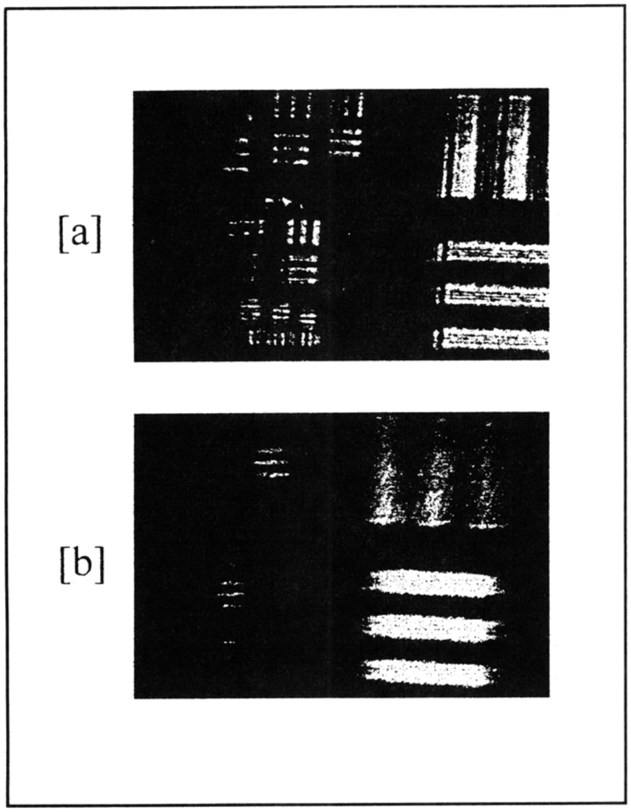

Figure 15. Illustration of the optical quality of a thick hologram made of PDA, when an Air Force resolution chart image is used as the read beam: (a) transmitted image, and (b) diffracted image.

1.4.2 Cryogenic, Four-Dimensional Memory Using Persistent Spectral Holeburning in Organics

As mentioned above, optical memory using persistent spectral holeburning (PSHB) can have a storage capacity that can be higher than that of volume holography alone by a factor of as high as 10^7. This increase comes at the cost of increased complexity and cost. First, the medium has to be kept at the liquid helium temperature for the life of the memory. Second, in order to take full advantage of the capacity, lasers have to be as narrow as 1 kHz.

In order to make a PSHB memory that can be practically usable, we have chosen to use a medium that is somewhat modest in its objective, thereby simplifying the system. Specifically, we use an organic dye called Clorin-e_6, embedded in a thick sample of polystyrene. The absorption is peaked around 665 nm, with an inhomogenous width of 10 nm, corresponding to 6.8 THz. The homogeneous width is about 1.7 GHz, so that the number of spectral holes is about 4 X 10^3. An externally stabilized tunable semiconductor laser made by Micracor® is used to access all of these holes. The system can operate at 10 K, so that a recirculating cryostat can be used. Due to the compact size of the recirculating cryostat, the sample size of the hologram can not be very big. Still, for a 5 mm-thick sample with a 3 cm-diameter, the storage capacity can easily exceed 100 Terabytes, with an access time of 1 Gbit/sec.

One of the key issues in this project is the preparation of a thick hologram that is free from spatial inhomogeneity, and has excellent optical quality. We have developed a special procedure, involving inert atmospheres, vacuum boiling, and variable-pressure molding to develop samples that meet these criteria. To check for flatness, we have inserted the sample (2 cm diameter, and 2 mm thick) in one arm of a Michaelson interferometer. The resulting fringes (figure 16a) show that the combined phase variation over the volume and the two surfaces is less than $\lambda/5$. We also transmitted an Air Force resolution chart image through this sample, with minimal scattering and distortions, as shown in figure 16b.

The next step is to insert the sample in the cryostat, and write a series of high density digital data, mutiplexed angularly as well as spectrally, with the goal of achieving a raw BER of 10^{-5}. Ultimately, our objective is to produce a complete storage system with a capacity of 100 Terabytes.

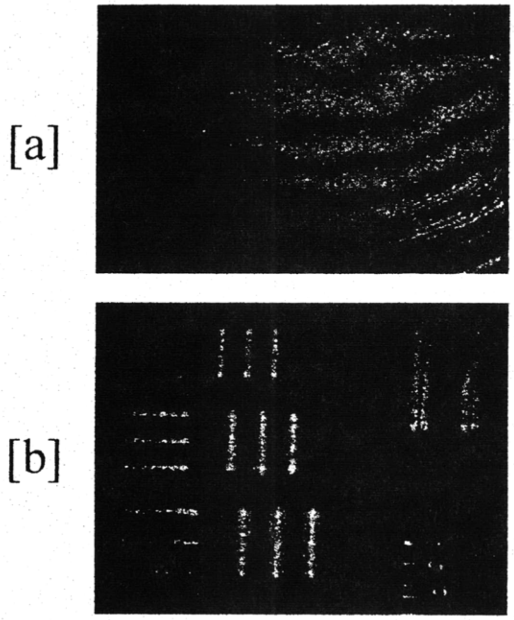

Figure 16. Illustration of the optical quality of a thick hologram made of chlorin-e_6 embedded in polystyrene: (a) Michaelson fringes with the hologram inserted in one arm, and (b) transmitted profile of an Air Force resolution chart image.

1.5 A Rubidium Atom Trap for Applications to Nanolithography Using Atom Interferometry

Sponsors

National Science Foundation
  Grant PHY-9312572
U.S. Air Force - Office of Scientific Research/
  DURIP
  Grant F49620-95-0510

Over the last decade, the computer industry has been revolutionazied by very large scale integrated circuits, with ever increasing number of transistors on a single chip, yielding powerful processors as well as high speed and high capacity random access memory. However, the number of transistors is ultimately limited by the resolution of lithographic techniques. One of the ways to circumvent the current limits is to perform lithography using atomic interferometry.

Last year, we reported experimental results of an experiment where blazed gratings produced by optical standing waves are used to split an atomic beam of metastable helium. Given the limits of the optical power available from the LNA laser, we were able to demonstrate a splitting of ± 20 $\hbar$k, where $\hbar$k is the linear momentum of a photon.[43] In principle, however, this process is capable of producing splittings as large as ± 200 $\hbar$k.

Currently, we are working on using this scheme to create such a beam splitter using rubidium atoms. The high power available from a Ti:Sapphire laser makes it possible to achieve the large amount of splitting mentioned above. Once the split atoms are recombined, they interfere to produce fringes. For the ± 200 $\hbar$k splitting, the fringe spacing is less than 2 nm. By using mutiple zones of beam splitting, it possible to get fringes that are less than a nanometer wide.

We will use this process for two purposes. First, this would represent the best atomic interferomter yet. As such, we will make measurements of fundamental constants such as the value of $\hbar$m, which in turn is used to determine the fine structure constant to a greater degree of precision than the current value. The interferometer can also be used to measure the value of the acceleration due to gravity, and to measure general relativistic effects such as the Lenz-Thirring rotation. For this application, it is enough to have only a few fringes produced by the interference. Therefore, a moderate degree of transverse and longitudinal coherence is enough. However, we still need a high atom flux in order to maximize the signal-to-noise ratio. Both of these objectives are best met by a supersonic beam. Such a beam is currently under construction and will be operational in a few months.

Second, we will use this scheme to demonstrate two dimensional structures with a resolution of less than 2 nm. Initially, the structure will consist of a two-dimensional pattern of rubidium atoms. Such a pattern can be transferred to almost any other atoms of metal or semiconductor, using self-assembled-monolayer techniques. However, in order to maximize the usefulness of this approach to lithography, it is necessary for the atomic beam to have a coherence volume (defined as the product of the coherence lengths in three dimen-

---

[43] K. Johnson, J.D. Paul, A. Chu, M.S. Shahriar, K. Berggren, and M.G. Prentiss, "A Large Angle Coherent Atomic Beam Splitter without a Magnetic Field," *Opt. Lett.* 20: (1995).

sions) as large as possible. In order to achieve this objective, we will use subrecoil, three-dimensional Raman cooling techniques, developed[44] and demonstrated[45] in part by us over the last few years. As a source, we will use atoms initially held in a magneto-optic trap.

We have constructed such a trap, and have trapped both isotopes of rubidium. Figure 17 shows the fluorescence profile of a trapped ensemble of ^{85}Rb atoms. Preliminary measurements indicate a temperature of about 80 mK, and a density approaching 10^{10} cm^{-3}. Next, we plan to perform three dimensional, subrecoil Raman cooling to generate a source of atoms suitable for the interferometer.

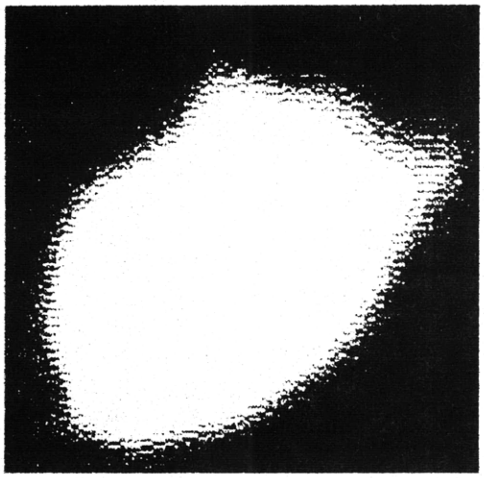

Figure 17. Fluorescence image profile of our magneto-optic trap containing ^{85}Rb atoms.

1.6 Fiber-Optic Damage Detection

Sponsor

Idaho National Energy Laboratory

Project Staff

Niell G. Elvin

1.6.1 Problem Statement

In the United States alone, billions of dollars per year are spent on the inspection and repair of existing structural components. In advanced composites, the nondestructive evaluation techniques which are used for damage monitoring tend to be expensive and unreliable. Fiber-optic sensors can potentially offer a solution to existing structural integrity monitoring problems due to their high sensitivity, low weight, immunity to electromagnetic interference such as lightning, continuous monitoring capabilities, ability to detect distributed strains, and relatively low cost. This proposed research will focus on theoretical electro-mechanical analysis and experimental verification to provide guidelines for the design and placement of fiber-optic sensors.

The factors effecting fiber-optic system design are (1) crack length (or opening), (2) relative position of the fiber sensor to the crack, (3) orientation of the fiber relative to the damaged zone, (4) mechanical properties of the fiber and structural material, and (5) optical properties of the fiber.

1.6.2 Research Methodology and Proposed Future Work

In our previous work,[46] a novel moving load method was described which allows for the detection of the extent and position of delamination damage in composite materials. Extent and position of damage

---

[44] M.S. Shahriar, P.R. Hemmer, M.G. Prentiss, P. Marte, J. Mervis, D.P. Katz, N.P. Bigelow, and T. Cai, "Continuous Polarization-Gradient Precooling Assisted Velocity Selective Coherent Population Trapping," *Phys. Rev. A. (Rapid Comm.)* 48: R4034 (1993); M.S. Shahriar, D.P. Katz, A. Chu, J. Mervis, M.G. Prentiss, T. Cai, N.P. Bigelow, P. Marte, P. Zoller, and P.R. Hemmer, "Cooling and Confinement Assisted Velocity Selective Coherent Population Trapping Using Standing Wave Raman Excitation," *Laser Phys.* 4: 848 (1994).

[45] M.S. Shahriar, M.T. Widmer, M.J. Bellanca, E. Vredenbregt, and H.J. Metcalf, "Observation of Cooling Assisted Velocity Selective Coherent Population Trapping," International Quantum Electronics Conference, *OSA Technical Digest Series,* Vol. 9 (Washington, D.C.: Optical Society of America, 1994), p. 238.

[46] N.G. Elvin, "Damage Detection in Civil and Aerospace Structures with Fiber Optic Sensors," S.M. thesis. Dept. of Civil Eng. and Dept. of Aero. and Astro., MIT, 1995; N.G. Elvin, and N. Leung, "Feasibility Study of Delamination Detection with Embedded Optical Fibers," submitted to *J. Intell. Mat., Syst. Struct.*

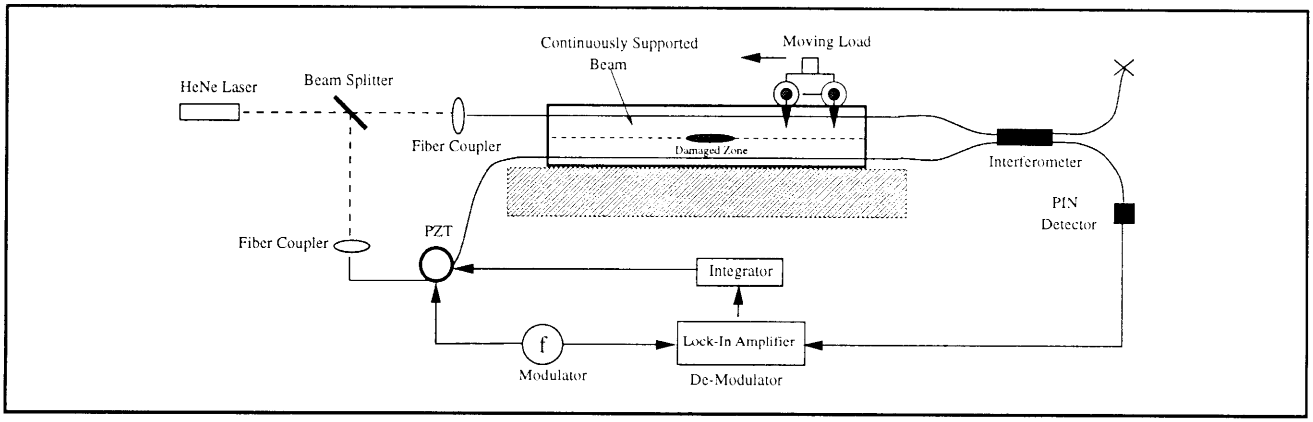

Figure 18. Schematic representation of moving load method and fiber optic sensor scheme used to detect delamination damage.

can be garnered by the monitoring of the integrated strain while moving a load over the delaminated site. Figure 18 shows a schematic representation of a Mach-Zender interferometer with active servohomodyne demodulation which can be used to determine the strain differences of cracked and uncracked structural component.

The scope of the present work will be to: (1) extend the existing mechanical analysis to include analysis capabilities of damaged multilayer composite materials, (2) test further the servohomodyne demodulated Mach-Zender interferometer, (3) compare experimental and theoretical results, and provide design guidelines for delamination detection.

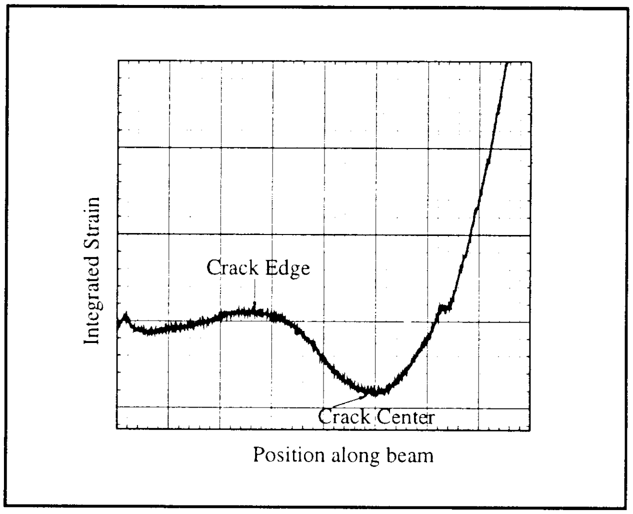

Figure 19. Initial experimental results. Crack position and length as indicated.

1.6.3 Initial Results

Figures 19 and 20 show some initial experimental and theoretical results for a continuously supported damaged beam. Note that the peaks in the diagrams show accurately the position and extent of the damaged zone.

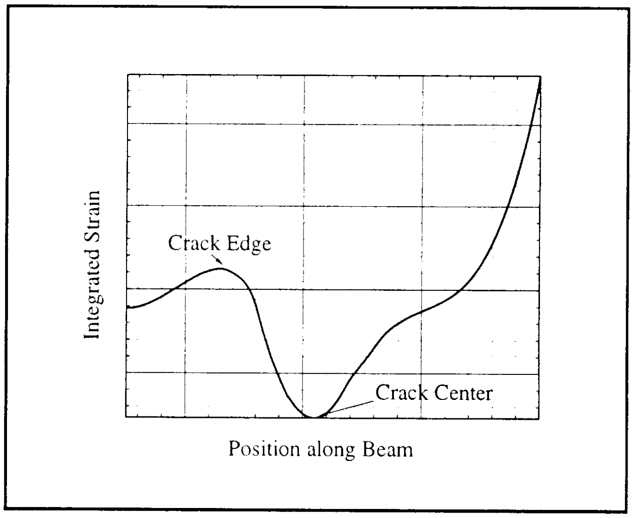

Figure 20. Initial theoretical results. Finite Element Method is used to calculate the change in sensing arm length.

1.6.4 Publications

Elvin, N.G., and N. Leung. "Feasibility Study of Delamination Detection with Embedded Optical Fibers." Submitted to *J. Intell. Mat., Syst. Struct.*

1.7 Demonstration of a Fiber-optic Quench Detector for Large Superconducting Magnets

Sponsor

MIT Plasma Science and Fusion Center

Project Staff

Dr. Stephen P. Smith

The next generation magnetic confinement fusion machines (tokamaks) will use superconducting, rather than conventional, magnets for confining and heating the plasmas. These magnets can be longer than a kilometer and typically are cooled using a forced flow of liquid helium through the conduit which surrounds the superconducting cable. The detection of a quench, i.e., a section of the magnet going normal, is very important since the local heating due to an undetected quench could lead to permanent magnet damage. Thus, a quick and reliable way of detecting such quenches is very important.

One novel method for detecting quenches in such a magnet is to include an optical fiber with the superconducting cable inside the conduit. Since the optical fiber is in close contact with the cable, any local heating of the cable also causes heating of the fiber, which can be detected interferometrically.

This technique has been sucessfully demonstrated in laboratory scale experiments[47] and now has been demonstrated in a 100 meter-long cable.[48]

This experiment, called QUELL, is a part of an international scientific collaboration on fusion research between the United States, Japan, the European Union, and the Russian Federation, called ITER. The test cable was made in Japan including sensors provided by the US, and was tested at the Sultan magnet facility, a part of the EPFL, in Switzerland.

For this experiment, techniques had to be developed for embedding the fiber inside the superconducting cable and withstanding the numerous manufacturing steps required to build the sample, including a heat treatment with a temperature above 600 degrees C for over 200 hours, and also cooling to 4 K during the experiment. In order to survive the heat treatment, single mode optical fiber with a copper jacket, instead of a conventional plastic jacket, was selected. For additional mechanical protection, this fiber was covered with a glass braid and then encased in a stainless steel capillary tube.

As shown in figure 21, detection of quenches in the QUELL sample was done by using the embedded fiber as one arm of a Mach-Zehnder interferometer. By measuring the phase difference between the light in embedded fiber, labeled the Sense arm in the figure, and a Reference arm held at constant temperature, the elongation of the Sense arm due to the heating associated with a quench can be measured. For these experiments, a frequency difference was introduced between the two arms of the interferometer using acoustooptic modulators (AO). Thus, when there was no heating, the output of the interferometer was a constant frequency. When the sense fiber was heated at a constant rate this output frequency would increase by a fixed amount, proportional to the rate of heating. This output frequency was measured and recorded as the output of this quench detector.

---

[47] S. Pourrahimi, W.C. Guss, J.V. Minervini, D.B. Montgomery, N.T. Pierce, J.H. Schultz, S.P. Smith, and S. Ezekiel, "U.S. Contributions to the Development and Calibration of Quench Detectors for the ITER QUELL," *Proceedings of the Applied Superconductivity Conference,* Boston, Massachusetts, October 17-20, 1994.

[48] S. Pourrahimi, S.P. Smith, J.V. Minervini, J.H. Schultz, A. Anghel, G. Vecsey, and Y. Takahashi, "Performance of the U.S. Quench Detection System in the QUELL Experiment," *Proceedings of the Applied Superconductivity Conference,* Pittsburg, Pennsylvania, August 26-30, 1996.

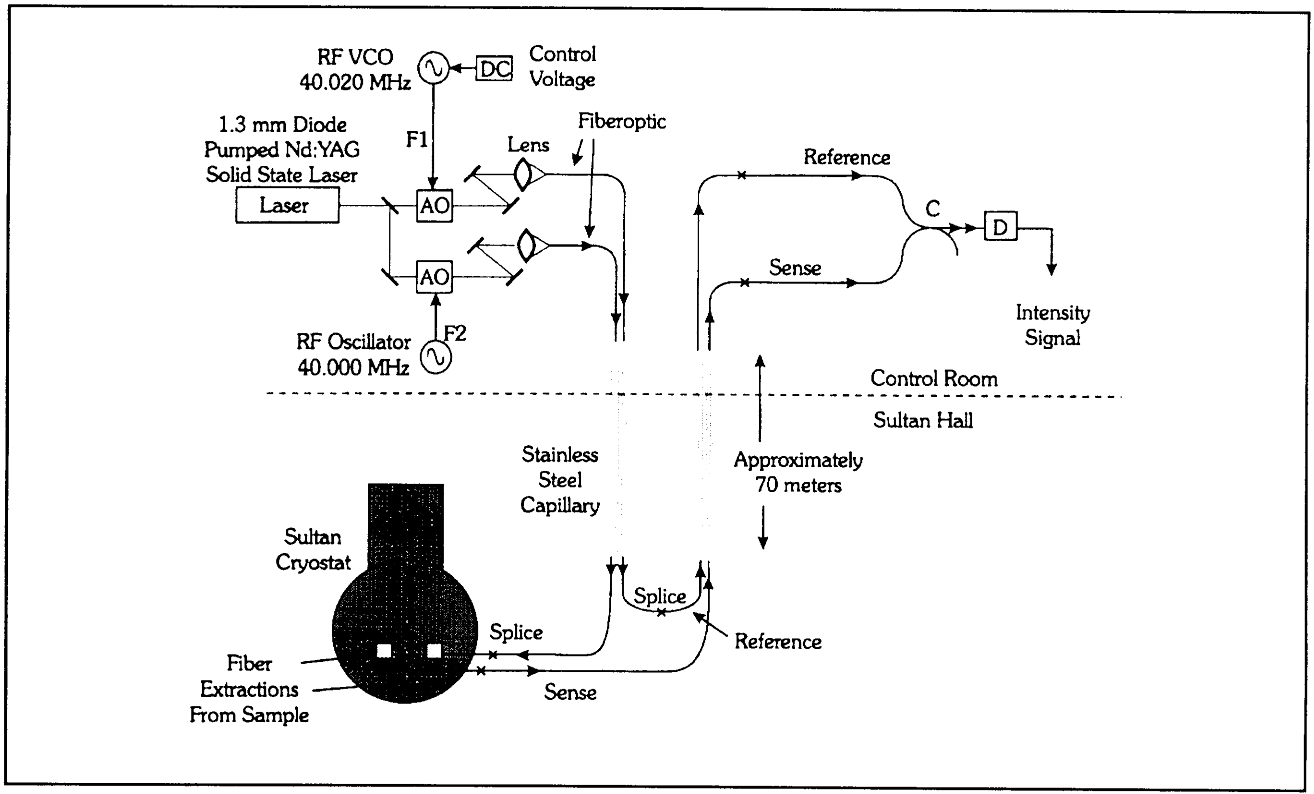

Figure 21. Schematic diagram of the installation of the optical fibers for the QUELL experiment.

Finally, neither an active polarization adjustment scheme nor a polarization insensitive detection scheme was used. It was found that the polarization of the sensing arm was quite stable except during current ramp up and down of the sample.

Figure 22 shows typical data from a long initial normal zone (INZ) quench with a sample current of 12 kA. Starting in the upper right plot and moving clockwise, the frequency output from the fiber-optic instrumentation is shown, then the heater current used to initiate the quench, then the current in the sample and finally the sample voltage as measured by the cowound voltage tap. For this quench, a long resistive heater pulse is triggered at the 2 second mark of the figure to initiate the quench in the sample, and due to the long thermal time constant of this heater, the first resistive voltage was seen at about 3.5 seconds. As seen in the figure, there is no response of the fiber-optic sensor to the heat pulse, but almost coincident with the appearance of resistive voltage a change is noted in the fiber-optic signal, and this change continues to grow until the sample is ramped down at approximately 6 seconds. The quantization of the fiber-optic frequency signal is due to the use of a counter to measure the frequency (τ = 0.1 sec, resolution 10 Hz).

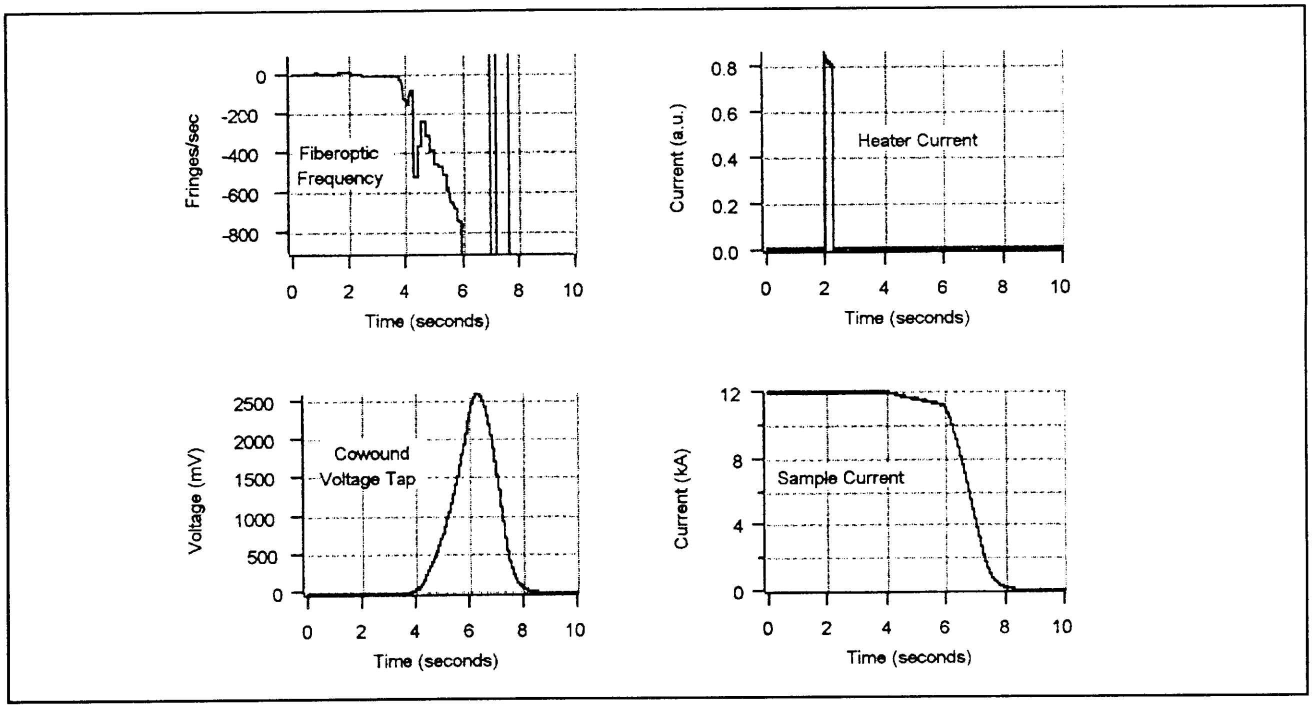

Figure 22. Typical response of the fiber-optic sensor to a long INZ quench. Clockwise from upper left, frequency from the fiber-optic instrumentation, heater current which starts the quench, sample current, and sample voltage measured by the cowound voltage tap.

Figure 23 shows a typical short INZ quench with a sample current of 8 kA again with the (starting in the upper left and moving clockwise) fiber-optic frequency, heater current, sample current, and sample voltage shown. The heater pulse occurs at 2 seconds again, but the sample does not quench until approximately 7 seconds. Also seen in this figure is that there is no fiber-optic sensor response to the heater pulse, and it is not until a resistive voltage is observed that any significant change in the fiber-optic signal is observed.

Here, due to the much shorter initial normal zone, the integral of the temperature change as well as the resistive voltage increase much more slowly. This makes short length quenches more difficult to detect, but due to the very small heated zone, the maximum temperature for a given quench threshold (voltage or fiber-optic) is higher.

Another important piece of data is the difference between a "near quench" and a quench. Figure 24 shows the results of two heater pulses on the QUELL sample taken a few minutes. In the left plots, the heater pulse was not quite large enough to quench the sample as shown by both the fiber-optic sensor response and the cowound voltage tap. In the right plots, the heater energy was increased by approximately 2.5 percent causing the sample to quench with a short INZ as shown by the resistive voltage. As easily seen in the upper plots, the difference between a quench and a heater pulse is quite dramatic for the fiber-optic sensor. Over the duration of the QUELL experiment, almost 90 quenches and over 150 non-quench data runs were recorded. In all these runs, the fiber-optic quench detector was able to correctly determine whether or not a quench had occurred before the cable had exceeded its designed temperature range. This demonstrates the ability of optical fibers to quickly and reliably detect quenches in large superconducting magnets.

While the fiber-optic quench detector demonstrated the ability to reliably detect quenches in a mechanically and electrically noisy environment, there are several areas in which further developmental work is needed. One important area is strain sensitivity reduction. In a magnet that is ramped quickly, the strain sensitivity of the fiber-optic quench detector would have to be compensated for and a number of techniques have already been explored and demonstrated in the laboratory for this effect. These techniques range from very simple, such as using the measured rate of change of magnet current, to the more elegant, such as using special fiber-optics. In conjunction with this effort, it may also be possible to increase and further tailor the temperature sensitivity of the fiber-optic by applying layers of different jacket materials.

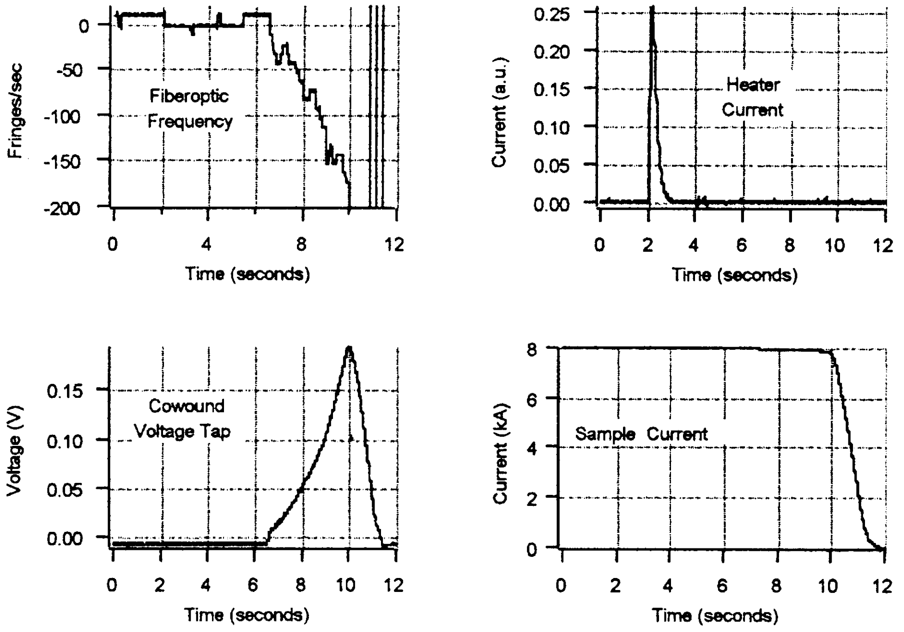

Figure 23. Typical response of the fiber-optic sensor to a short INZ quench. Clockwise from upper left, frequency from the fiber-optic instrumentation, heater current which starts the quench, sample current, and sample voltage measured by the cowound voltage tap.

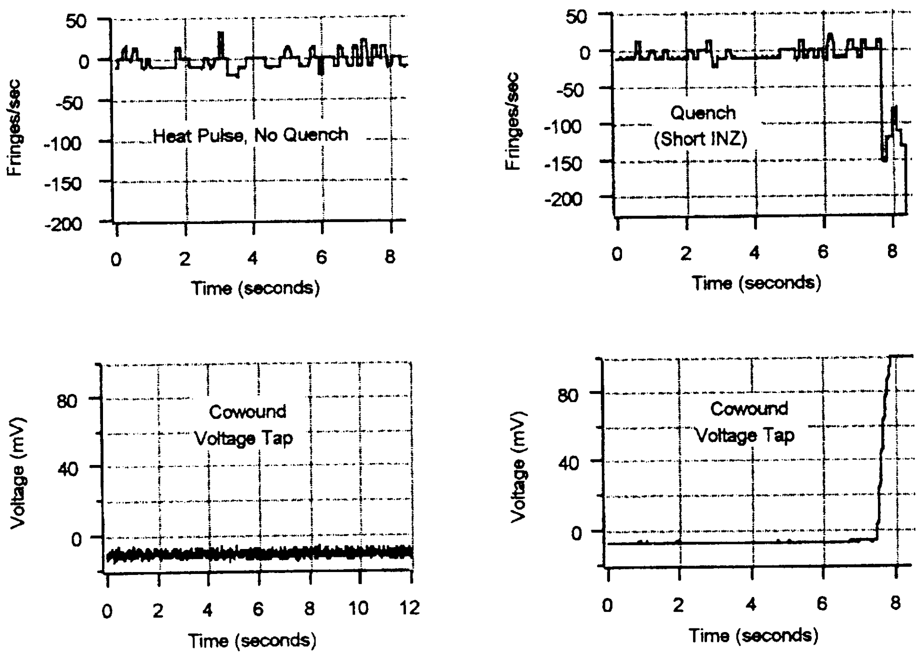

Figure 24. Response of the fiber-optic sensor to a "near" quench heater pulse (left pair) compared with the response to a short INZ quench (right pair).